Magnetic amino-sulfonic dual sorbent for uranyl sorption from aqueous solutions – Influence of light irradiation on sorption properties

Mohammed Hamza, Eric Guibal, Yuezhou Wei, Amr Fouda

Magnetic amino-sulfonic dual sorbent for uranyl sorption from aqueous solutions – Influence of light irradiation on sorption properties

Mohammed F. Hamza [a,b], Eric Guibal [c,*], Yuezhou Wei [a,d,**], Amr Fouda [e]

[a] School of Nuclear Science and Technology, University of South China, Hengyang 421001, China
[b] Nuclear Materials Authority, POB 530, El-Maadi, Cairo, Egypt
[c] Polymers Composites and Hybrids (PCH), IMT Mines Ales, Alès, France
[d] School of Nuclear Science and Engineering, Shanghai Jiao Tong University, Shanghai, China
[e] Botany and Microbiology Department, Faculty of Science, Al-Azhar University, Nasr City, Cairo 11884, Egypt

A B S T R A C T

The association of magnetite microparticles with bi-functional amino-sulfonate polymer (obtained by conden-sation of guanidine and amino hydroxynaphthalene sulfonic acid, mediated by formaldehyde) allows synthe-sizing a magnetic composite sorbent (M– GANS). The sorbent bearing both amine and sulfonate groups is efficient for uranyl sorption at pH 4–5. The sorption isotherms are successfully fitted by the Temkin equation, while kinetics is controlled by the pseudo-first order rate equation. The sorption properties are increased by UV irradiation in terms of both sorption capacity (by 25 %, up to 1.25 mmol U g^{-1}) and kinetics. The sorption occurs on both amine and sulfonate groups; the improvement in sorption properties under UV irradiation is tentatively assigned to the photo-reduction of uranyl species (mediated by magnetite particles and amine groups from polymer layer). The UV irradiation improves the selectivity of M–GANS for uranium against other metal ions, tested on both synthetic and real solutions. This improvement can be correlated to the higher propensity of uranyl to be photo-reduced compared with investigated competitor ions. The recycling of the sorbent was suc-cessfully tested for five successive cycles of sorption and desorption (stably complete): the loss in sorption performances is slightly reduced (less than 1.5 % at the fifth cycle) under UV irradiation compared with experiments performed under dark conditions (loss close to 4.2 %). The uranium peroxide precipitate obtained at the end of the treatment of acid leachate of ore shows higher purity when UV irradiation was applied.

Keywords:

An efficient magnetic composite sorbent was synthesized by incorporation of magnetite nanoparticles into polymer matrix (obtained by formaldehyde polycondensation of guanidine and amino hydroxynaphthalene sulfonic acid)
UV irradiation allows to both increase uranium sorption capacity and enhance uptake kinetics
Temkin equations fitted sorption isotherms while uptake kinetics are successfully modeled with the pseudo-first order rate equation
The sensitivity of uranyl ions to reduction explains the complementary metal sorption and enhanced selectivity under UV irradiation for both synthetic and complex industrial solutions
UV exposure improves the stability of sorption properties at recycling (uranium being fully desorbed using nitric acid solution)

1. Introduction

The increasing constraints on the preservation of the environment and the growing demand for securing sources of strategic metals are strong incentives for the development of new processes and new materials targeted to the recovery of metals from dilute effluents and secondary resources (tailings, marginal ores, wastes, etc.). Conventional techniques such as precipitation, solvent extraction, membrane processes may face environmental, technical, and/or economic limits (production of huge amounts of contaminated sludge that are poorly valorizable, difficulty to reach the standards for discharge to the environment, or excessively expensive costs). Sorption processes represent an alternative for the recovery of uranium from dilute effluents [1]. Many types of sorbents have been tested for metal sorption (including U (VI) recovery) such as mineral sorbents [2,3], carbon-based sorbents [4], porous metal-organic framework [5,6], resins [7–11], and materials of biological origin [12–16].

The strong affinity of uranium for sulfonate groups [17–19] was a strong incentive for designing new resins bearing strong cation exchange functionalities [8,10,11,20–23]. Sulfonation of composite was also used for designing sorbents for the recovery of rare earth elements: for example, algal biomass/polyethylenemine beads were functionalized by sulfonation for recovering scandium, cerium and holmium [24]. The recovery of uranium using ion-exchange and chelating resins is widely documented, showing the possibility to use numerous functional groups [25,26,8]. Amine groups (including primary, secondary, tertiary and

* Corresponding author.
** Co-corresponding author.
E-mail addresses: eric.guibal@mines-ales.fr (E. Guibal), yzwei@usc.edu.cn (Y. Wei).

quaternary groups) or sulfonic acid bearing resins have been investigated for uranyl recovery. The bi-functionalization of resin has also shown significant enhancement in sorption properties (sorption capacities, selectivity, etc.) due to modulations in acid-base properties, steric effects, and arrangement of sorption site for accommodating target metal ions [27,28]. For these reasons, the sorbent investigated in this study was developed on the concept of bi-functionalization (with grafting amine groups, and sulfonic groups). The urea-formaldehyde resins have also received a great attention to the readily reaction of the precursors (through methylolation followed by condensation) [29]; the presence of amine groups of these resins opens also many possibilities for post functionalization. Herein, by analogy, urea has been substituted by guanidine: the similar structure (imine instead of carbonyl) guarantees a similar reactivity toward formaldehyde; the presence of another nitrogen site bears additional binding group. On the other side, 7-amino-4-hydroxy-2-naphtalenesulfonic acid (ANS) bearing an end-amine groups can also react with guanidine by the polycondensation reaction. This precursor brings an end-sulfonic acid group, which insures the bi-functionality of the final sorbent. The direct polycondensation of guanidine and ANS allows reaching a high density of amine and sulfonic groups.

In addition, the observation of the effect of light on the variability of uranium sorption performances allows identifying the contribution of photo-mediated reduction of U(VI) into U(IV). Incorporating an aromatic compound as source of sulfonic group (in ANS) favors this photoreactivity [30]. The elaboration of the composite (by incorporation of magnetite nanoparticles allows decreasing the size of sorbent particles (with higher specific surface area) while maintaining readily solid/liquid separation at the end of the sorption process. These interesting properties constituted one of the rationales for designing GANS sorbent (guanidine-amino-hydroxy-naphtalenesulfonic polymer), which was synthesized in this work by the one-pot thermal reaction of guanidine (bearing two primary amine group and an imine bond) and 7-amino-4-hydroxy-2-naphtalene sulfonic acid (ANS) in the presence of formaldehyde (promoting the condensation of the polymer). Formaldehyde contributes to the linkage of amine groups of guanidine with the amine groups on ANS, by analogy with the synthesis of urea-formaldehyde resins: methylolation (electrophilic substitution) followed by condensation (water loss). Formaldehyde polycondensation reaction may have some problems associated with the stability of the polymer (VOC release reported in in building facilities [31], and relative sensitivity to hydrolysis [32]). However, this is compensated by several advantages, such as fast-curing, water solubility (for reaction), and low price.

Sorption processes involving organic matrices are frequently facing kinetic problems associated with strong resistance to intraparticle diffusion. In order to manage these problems, the solutions may consist in: (a) expanding the structure (porogen action, expansion of the polymer network through controlled drying procedures, etc.), or (b) decreasing the size of sorbent particles (reduction of the diffusion path, which allows reducing the time required for saturating the internal reactive groups). In the case of size reduction, one of the main drawback is associated with the difficult solid/liquid separation at the end of the sorption process (requiring complex separation processes and precluding the use of the sorbent in fixed-bed column). One of the solution consists in designing magnetic sorbents (which can be readily separated by magnetic field). Different strategies can be adopted for the preparation of magnetic sorbents: (a) in-situ synthesis of magnetite nanoparticles in the polymer network [33], (b) embedment of pre-synthesized magnetite nanoparticles during the synthesis of the sorbent [34], or (c) aggregation of magnetite NPs with polymer by high-energy milling [35]. Herein, the applied strategy is based on the incorporation of pre-formed magnetite NPs into GANS during the synthesis of the polymer (embedment strategy).

The magnetic sorbent (i.e., M−GANS) is tested for uranium recovery from aqueous solutions. Preliminary tests showed a variability in sorption performances when varying experimental conditions, more specifically associated with light exposure. This was the motivation for carrying out the impact of light exposure on the sorption properties.

Though some metal ions (such as Cr(VI), [36]) have higher sensitivity to reduction phenomena, uranium(VI) can be reduced in soil through the action of sulfate-reducing bacteria, organic ligands [37] or iron-based minerals [38]; as one of the mechanisms involved in ore mineralization (geochemistry). Similar reducing mechanisms have been reported in the interpretation of uranyl binding onto zero-valent iron sorbents [13,39,40], which contribute to metal precipitation. Contrary to chemical and biochemical mechanisms that were regularly reported in the literature, the photoreduction of uranium has retained much less attention. Guibal et al. [41] characterized the effect of UV irradiation on the complexation of uranyl with soluble glucosamine and the binding of U(VI) onto chitosan (under aerobic and anaerobic conditions); with promotion of uranium precipitation (associated with pH variation). More recently, Chen et al. [42] described the synthesis of functionalized metal-organic frameworks (by incorporation of Ni(II)-centered porphyrin ligands into UiO-66-NH_2 support). This functionalization enhanced the reduction of U(VI) into U(IV), which can be readily removed; this modification contributed to the increase of uranium sorption (notably in seawater samples). Liao et al. [39] also evaluated the beneficial effect of U(VI) reduction on the sorption properties of zero-valent iron/titanium. Inspired by these mechanisms and their impact on metal binding, this work contributes to evaluate the impact of different mode of light exposure (dark, visible light, and UV light) on the binding of U(VI). After characterizing the sorbent through BET, VSM, TGA, FTIR, and titration, U(VI) sorption properties by M−GANS are investigated with a special focus on the effect of pH, uptake (and desorption) kinetics, sorption isotherms, comparing the respective effects of dark exposure, visible, and UV irradiation modes. The impact of irradiation mode is also carried out in terms of recyclability of the sorbent. Finally, M−GANS is incorporated in a combination of treatments for recovering uranium from acidic leachate of an ore sample. The leachate is first treated onto a commercial ion-exchange resin (Amberlite IRA-400). M−GANS sorbent is used for the recovery of residual uranium from pre-treated eluate (after intermediary precipitation step at pH 5).

2. Materials and methods

2.1. Materials

Uranyl nitrate hexahydrate, ($UO_2(NO_3)_2{\cdot}6H_2O$), was purchased from SPI Supplies (West Chester, PA-USA). Guanidine hydrochloride (≥99 %), 7-Amino-4-hydroxy-2-naphthalenesulfonic acid (≥90 %), formaldehyde (37 %), and sodium hydroxide (≥99 %), were obtained from Sigma-Aldrich (Taufkirchen, Germany). Glacial acetic acid, magnesium chloride hexahydrate (≥99 %), sodium chloride (≥99 %), calcium chloride (≥99 %), aluminum chloride hexahydrate (95 %), and ferric chloride, ($FeCl_3$, ≥ 99 %) were supplied by Guangdong Guanghua Sci-Tech Co., ltd. (Guangdong, China). Ferrous sulfate heptahydrate ($FeSO_4{\cdot}7H_2O$; ≥ 99 %), acetone (≥99 %) and ammonium ferric sulfate dodecahydrate ($(NH_4)Fe(SO_4)_2{\cdot}12H_2O$; ≥ 99 %) were purchased from Shanghai Makclin Biochemical Co., Ltd. (Shanghai, China). Amberlite IRA-400 (the anion exchanger used for the pretreatment of leachate) was purchased from Rohm & Hass Co. (Philadelphia, PA, USA).

2.2. Synthesis of M−GANS

2.2.1. Synthesis of magnetite nanoparticles

Nano-sized magnetite particles were produced by the so-called Massart method [43] (thermal precipitation). Five grams of ferrous sulfate ($FeSO_4{\cdot}7H_2O$), and 17.35 g of ammonium ferric sulfate ($(NH_4)Fe(SO_4)_2{\cdot}12H_2O$) (Fe(II)/Fe(III) molar ratio: 1:2) were dispersed in 50 mL of solution (until complete dissolving). The temperature of the mixture was maintained to 50 °C for 60 min under strong agitation (190 ± 5

rpm). The pH was then controlled to 11 using 5 M NaOH solution. Magnetite nanoparticles were magnetically collected and air-dried at 50 °C for 5 h. Finally, the magnetic nanoparticles (M) were alternatively washed with water and acetone; final air-drying was operated at 55 °C, overnight.

2.2.2. Synthesis of magnetic sorbent

Guanidine hydrochloride (5 g, 99 % purity; 51.8 mmol) was dissolved in demineralized water (50 mL) and distributed into a three-neck flask (100 mL, equipped with an agitator, a condenser, and a thermometer). In a second step, 7-amino-4-hydroxy-2-naphthalenesulfonic acid (12 g, 90 % purity; 45.1 mmol) was added into the reactor under continuous stirring; formaldehyde (4.9 mL, 49.6 mmol) was then dropped, together with three successive fractions of glacial acetic acid (0.5 mL, pH kept close to 3). Magnetic nanoparticles (7.5 g) were then introduced into the reactor under stirring (195 ± 5 rpm). The temperature was risen to 90 °C for 5 h. The black precipitate (magnetically collected, 19–20 g, d.w.) was washed with water and acetone before being air-dried at 65 °C for 10 h to produce M− GANS sorbent (See Scheme 1). Weight variation and mass balance on molar concentrations indicate that the degree of polymerization is relatively weak (in the range 10–18 %).

2.3. Characterization of materials

The SEM and SEM-EDX analyses were performed for morphological and chemical composition detection. The analyses were performed using a Phenom ProX-SEM (Thermo Fisher Scientific, Eindhoven, Netherlands). The thermal decomposition of the sorbent was carried out using a STA 449 F3 Jupiter Netzsch TG-DTA analyzer (Netzsch Gerätebau HGmbh; Selb, Germany). The analysis was performed in nitrogen environment with a 10 °C min^{-1} temperature ramp. The functional groups of the sorbent, after metal loading and after elution were characterized using FT-IR spectra, acquired on IR-Tracer, 100-FT-IR Shimadzu spectrometer (Shimadzu Corporation, Kyoto, Japan). The samples were firstly dried before grinding (and designed as KBr disk) and finally analyzed in the IR-Tracer 100-FT-IR spectrometer (Shimadzu Corporation, Kyoto, Japan). The porosity and the surface area were calculated from N_2 adsorption/desorption isotherms: samples were immersed in N_2 for 4 h at 130 ± 5 °C, analyses were acquired on a TriStar II surface area and porosity analyzer (Micromeritics, Norcross, GA, USA). The BET equation was used for the determination of specific surface area, while BJH-method was employed for quantifying porous volume and pore size. Elemental analysis (C, H, N, O, and S) was carried out using a Vario EL cube element analyzer (Elementar-Analysensysteme; GmbH, Langenselbold, Germany). The magnetic properties (M−H loop) were analyzed using a Lake Shore 7410 vibrating sample magnetometer (VSM, Lake Shore Cryotronics, Westervill, OH, USA).

The pH-drift method was used for the determination of the pH_{PZC} value. Solutions (50 mL, with NaCl as background salt, 0.1 M solution) with initial pH_0 set to 1–11, were mixed for 48 h with a fixed amount of sorbent (m: 0.1 g). The final pH (i.e., pH_{eq}) was monitored with a pH-meter/ionometer S220 (Seven compact, Mettler Toledo, Shanghai, China). The pH_{PZC} value corresponds to the condition: $pH_0 = pH_{eq}$.

Major oxides in the ore sample were chemically analyzed using XRF technique (X-ray fluorescence with Nex CG Rigaku EDXRF-spectrometer, Rigaku Corporation, Tokyo, Japan). The REEs were analyzed by spectrophotometry (colorimetric technique according to Marczenko [44] using a UV–vis spectrophotometer; Shimadzu UV-160A, Shimadzu Corporation, Kyoto, Japan). The rare earth elements react with Arsenazo III solution (0.015 %, w/w); cerium was taken as the reference for global quantification. Uranium in the leaching liquor was analyzed using the oxidimetric titration technique against ammonium metavanadate and using diphenyl amine-4-sulfonic acid sodium salt as the indicator [45]. The trace elements (Zn, Cu, Cr, Ni, V, etc.) were determined by Unicam atomic absorption spectrophotometer-969 (AAS).

2.4. Sorption studies and modeling

The sorption properties were carried out in batch system. The metal-containing solution (volume, V, L; initial concentration, C_0, mmol U L^{-1};

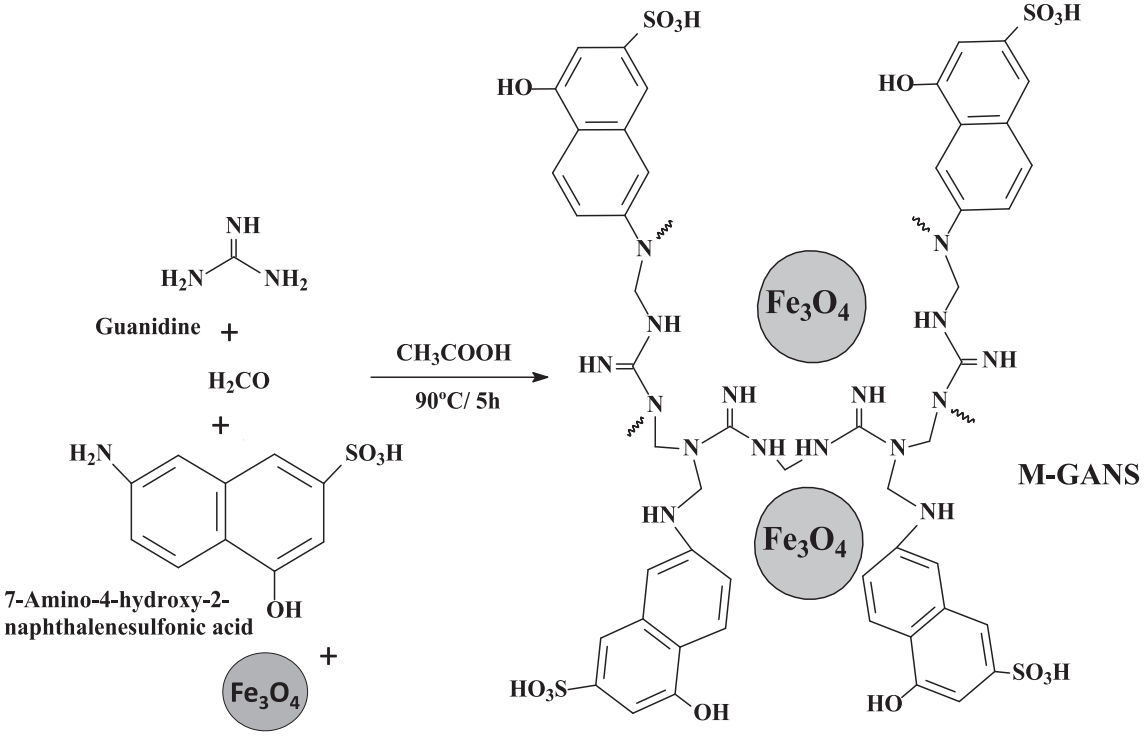

Scheme 1. Synthesis route for the preparation of M−GANS sorbent.

pH_0) was mixed with a fixed amount of sorbent (m, g; sorbent dose, SD = m/V; g L^{-1}). Agitation and temperature were set to v: 200 rpm and T: 21 ± 1 °C. The contact time was fixed to 48 h for sorption isotherms, while for uptake kinetics, samples were collected at fixed contact times. After withdrawing, the samples were filtered through membrane filter (pore size: 1.2 μm) and analyzed by ICP-AES (inductively coupled plasma atomic emission spectrometry, ICP-AES 7510, Shimadzu, Kyoto, Japan). Sorption tests were systematically duplicated; the average values (and standard deviations) are reported; these data confirm the good reproducibility of sorption properties.

The study of metal desorption was also performed in batch systems. Metal-loaded sorbent was mixed with 0.3 M HCl solution (SD: 2.0 g L^{-1}; time: 4 h; while sorption conditions: SD: 0.666 g L^{-1}; C_0: 0.434 mmol g^{-1}; pH_0: 5.0; time: 24 h. The recycling tests were performed on the same mode; a rinsing step (with deionized water) was systematically processed between each operation.

The sorption tests performed under UV light were carried out in closed box (with agitation system) equipped with 980 nm cw laser diode systems (Lambdawave, Wroclaw, Poland). The power was ≈ 0.84 W (with 8 mm^2 size beam).

Conventional models (reported in Tables S1 and S2, see Supplementary Information section) were used for the modeling of uptake kinetics (pseudo-first order and pseudo-second order rate equation, and resistance to intraparticle diffusion, Table S1) and sorption isotherms (Langmuir, Freundlich, Sips, Temkin, and Dubinin-Radushkevich equations, Table S2). The parameters were determined by non-linear regression analysis using Mathematica® facilities, and proprietary math notebook. The evaluation of the quality of the fits was based on the determination coefficient (i.e., R^2) and the Akaike Information Criterion (AIC, [46]).

2.5. Application to ore treatment

The sample used for testing M−GANS application in uranium recovery from complex effluent is a pre-treated leaching liquor. The pristine leaching liquor contained 168 mg U L^{-1} (pH 2.2–2.5), it was produced through the treatment of ore materials (330 mg U kg^{-1}) by sulfuric acid (100 g L^{-1}) with solid liquid ratio 1:2.2. Uranium leaching efficiency of the pristine ore material was about 96.7 %. After treatment with quaternary ammonium resin (Amberlite IRA 400) in column process, the outlet solution contained a residual concentration close to 23 mg U L^{-1}. Fifty L of leachate (after controlling the pH to 1.8–1.9) were percolated through fixed bed column (4-cm diameter, 60-cm height) filled with the ion-exchanger (200 g). This outlet solution still contained high concentrations of aluminum and iron (up to ≈11 g L^{-1}), which can strongly depreciate uranium binding (trace concentrations about 500 folds lower than major trivalent cations). A pre-treatment consisting of precipitation at pH 5 (using concentrated NaOH solution) was applied to sharply decrease their concentration. This residue of precipitation step was used for testing uranium recovery by M−GANS from complex effluent: the residual amount of uranium was close to 18.2 mg U L^{-1}. The sorption tests were processed in batch systems: contact time was set to 5 h; agitation velocity was fixed at 150 rpm with a sorbent dose (SD) of 0.4 g L^{-1}. Sorption performances were compared under visible and UV light exposure.

For the study of the desorption of uranium from loaded sorbent, M−GANS was mixed at 150 rpm for 5 h with a fixed volume of pre-treated leachate solution at pH_0 5 (C_0: 18.2 mg U L^{-1}); the sorbent dose was fixed to 0.4 g L^{-1}. The desorption was carried out using 1 M HNO_3 solution. The sorbent dose was 2 g L^{-1} and the contact time was set to 1 h. The pH of the eluate was raised to 2.5 (with 7 % NaOH solution, w/w; 0.5–0.6 mL) before adding H_2O_2 (130 v/v, 2.4–2.9 mL) for precipitating uranium, as $UO_4{\cdot}H_2O$ The yellow-precipitate was semi-quantitatively characterized using EDX analysis, after water rinsing.

3. Results and discussion

3.1. Sorbent characterization

3.1.1. Physical characteristics

Sorbent particles appear in Fig. S1 as irregularly shaped micro-objects (diameter ranging between 1 and 7 mm). Some particles are characterized as smoothed surfaces with sharp edges, while other appear as flaky clusters. There is a wide dispersion in both the size and the shape of the micro-particles. The textural characteristics are reported in Fig. S2. The N_2 adsorption/desorption isotherm corresponds to the Type IV profile, with a steep slope at high relative pressure (i.e., $p/p_0 \sim 0.9$). The hysteresis loop is close to the type H1 shape, which is associated with a narrow range of uniform mesopores [47]. Fig. S2b confirms this interpretation, the distribution of pores is roughly mono-modal (diameter around 700 Å); actually, the BJH methods allows establishing that the pore size was around 583 Å (based on adsorption branch) and 431 Å (for the desorption branch). This means that the material can be considered mesoporous, according to IUPAC classification [48]. However, the N_2 adsorption/desorption isotherms shows an unexpected second hysteresis when the relative pressure exceeds 0.98. The specific surface area reaches 69.4 m^2 g^{-1}, while the porous volume approaches 0.84 cm^3 g^{-1}.

The magnetization behavior of M−GANS sorbent is reported in Fig. S3. The saturation magnetization approaches 26 emu g^{-1}, with coercivity close to 97 G and weak retentivity (≈2 emu g^{-1}). In the case of magnetite particles, Petcharoen and Sirivat [49] reported saturation magnetization at 57.1 emu g^{-1} and coercivity close to 28.4 G; much lower values than those reported for bulk magnetite by Iida et al. (i.e., 93 emu g^{-1}) [50]. High values of coercivity are usually associated with ferromagnetic character at room temperature, while, on the opposite hand, low coercivity corresponds to superparamagnetic behavior [50]. It is noteworthy that Iida et al. [50] reported that superparamagnetic magnetite is produced using a mixture of Fe(II) and Fe(III) salts in the hydrolytic procedure, while ferromagnetic materials results from the direct thermal hydrolysis of ferrous salt. Herein, the synthesis was performed with both Fe(II) and Fe(III) salts, but the coercivity remains at high level (ferromagnetic behavior). Obviously, the coating of magnetite nanoparticles contributes to reducing the magnetization of the material [49]; this effect is even more marked in the case of magnetite incorporation in polymer matrices (like with M−GANS) [51,52], because of both the shielding effect and the decrease of the reduced fraction of magnetite in the composite material. However, the saturation magnetization is sufficient for promoting the solid/liquid separation of the sorbent from metal-containing solutions.

The study of thermal degradation (under N_2 atmosphere) is summarized in Fig. S4. The analysis allows quantifying the amount of magnetite in the composite sorbent (i.e., below 34 % based on the residual material at 900 °C). This fraction of magnetite may explain the order of magnitude of the saturation magnetization given by VSM analysis. In addition, the global degradation occurs through three successive stages: 28.6–314.8 °C (water release; counting for weight loss, WL: 16.6 %), 318.8–577.2 °C (depolymerization, degradation of ending groups, degradation of naphthalene groups; WL: 34.2 %), and 577.2–889.6 °C (degradation of the char, and change of the physical state of magnetite to hematite, [53]; WL: 14.9 %) [54,55]. The DrTG curve (Fig. 4b) shows a strong peak at 492.4 °C corresponding to the thermal degradation of functional groups and the de-polymerization of the material (with peaks at 228.7 °C, and 345.6 °C; in addition to the shoulder at 57.6 °C, associated with water release).

3.1.2. Chemical characteristics

Fourier-transform infrared spectroscopy is an efficient tool not only for characterizing the functional groups present on M−GANS but also for interpreting the interactions of the sorbent with uranyl ions. Fig. 1 compares the FTIR spectrum of pristine sorbent with the spectra of M−GANS exposed to pH 5 solution and uranyl solution (at the same pH).

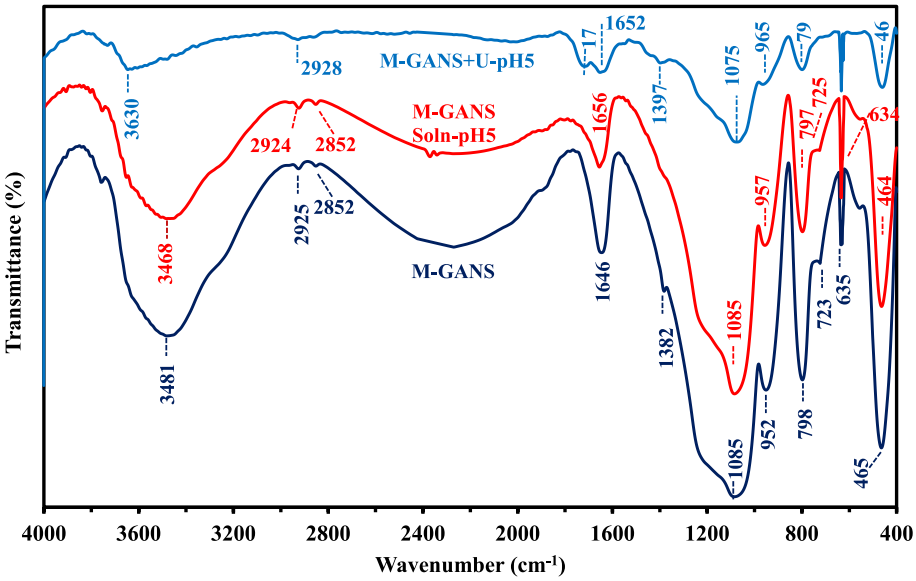

Fig. 1. FTIR spectra of M−GANS sorbent (pristine) and after contact with aqueous solution at pH 5 and U(VI) sorption at pH 5.

The comparison of pristine sorbent and pH 5-controlled material does not show significant differences. Under these mild conditions (pH 5), the functional groups are not subject to strong protonation/deprotonation effect. Table S3 summarizes the tentative assignment of FTIR peaks on the different materials. Therefore, the differences between pristine M−GANS and U-loaded sorbent can be directly related to the interaction of the metal ions with relevant functional groups. These differences are highlighted in Fig. S5. The band at 3481 cm^{-1} (overlapping of ν(O—H); ν(N—H)) is shifted to 3630 cm^{-1} after uranyl sorption, as an indicator of the modification of the chemical environment of amine groups [56] and/or the increase of the contribution of –OH groups (including hydrated species). After metal binding, a new band appears at 1717 cm^{-1} on the side of the band at 1646 cm^{-1} ($\nu(C{=}C)_{arom}$; δ(N—H) and ν(C═N) in hydrazine-based compounds, and guanidine): *N*-bearing groups are involved in uranyl uptake. Alternatively, this band can be assigned to sulfonic acid hydrate stretching [57]; meaning that sulfonic groups are also involved in metal binding. A weak band appears at 1397 cm^{-1} (with additional side shoulder), but the relative contributions may be masked by the weak composite band appearing at 1085 cm^{-1}, which is shifted to 1075 cm^{-1}. This band, which is attributed to ν(S═O) [58,59], is shifted with uranyl binding. The presence of uranyl may be generally identified by the appearance of a band at 919–920 cm^{-1} ($\nu_{as}(O=U=O)$ [56,60]); herein, the strong peak at 952–957 cm^{-1} ($\delta(C{-}H)_{arom.}$) mask the appearance of U = O vibration. Fig. S6 compares the spectra of pristine M−GANS, sorbent pre-treated with 0.3 M HCl solution, and the U-loaded sorbent after 0.3 M HCl desorption (at the fifth sorption/desorption cycle). The FTIR spectra are hardly modified after five recycling steps (Table S4); most of the changes concern shifts in characteristic bands (for example, the band at 1646 cm^{-1} moved to 1654 cm^{-1}). The limited amplitude of these changes tends to demonstrate that the sorbent remains remarkably stable despite the alternating contacts with mild (pH 5) and acidic solutions (0.3 M HCl). This stability can be correlated with the stable sorption properties (see Section 3.2.6.).

The elemental analysis (Table S5) confirms the high density of *N*-based reactive groups (equivalent to ≈10.5 mmol N g^{-1}) and sulfonic groups (≈3.15 mmol S g^{-1}). These data demonstrate the successful synthesis of the guanidine/7-amino-4-hydroxy-2-naphtalenesulfonic acid derivative. However, the analyzed N/S molar ratio does not exceed 3.3, while the suggested structure displays a theoretical ratio of four. This means that the number of guanidine groups in the skeletal chains is probably lower than represented in Scheme 1. Iron content is close to 17 %; this corresponds to ≈23.7 %, as Fe_3O_4. Compared to the residue at 900 °C (TGA characterization), which is close to 34 %; the residue may contain pyrolyzed fraction (not completely degraded, about 10 %). The semi-quantitative EDX analyses of the sorbent (raw and after uranyl sorption under exposure to different types of light) show substantial differences with elemental analysis (Fig. S7); EDX analysis is limited to surface composition (the depth of penetration of irradiation beam does not exceed a few tens of nanometers). These data show the substantial binding of uranium (which increases when the conditions of irradiation become more drastic). It is noteworthy that uranium binding is accompanied by the appearance of trace amounts of sodium (while Cl element disappears).

The global charge of the sorbent results from the competitive effects of amine groups, hydroxyl (in naphthalene rings) and sulfonic functions. While 7-amino-4-hydroxy-2-naphthalenesulfonic acid has very low pK_a value (predicted value close to -0.28 ± 0.40), guanidine has a pK_a value close to 13.71. The poly-condensation of guanidine with the naphthalene sulfonic derivative through formaldehyde gives a sorbent with pH_{PZC} values in the range 7.28–7.85 (Fig. S8). It is noteworthy that the light irradiation progressively shifts the pH_{PZC} toward lower values; however, the changes do not exceed 0.6 unit (between dark and UV exposure).

Experimental conditions were selected based on literature (found in the field or urea-formaldehyde resins); changing the molar ratio could probably affect the characteristics (and the properties) of condensed polymer. In the case of urea-formaldehyde resins, important parameters have been regularly reported [61]: molar ratio between urea and formaldehyde, reaction time, temperature, and pH. Herein, the molar concentrations of the coupling agent and precursors formaldehyde/guanidine/ANS are 0.0496/0.0518/0.0451 mol (i.e., almost equimolar) means that the precursors are in excess compared with the coupling agent (≈2:1). This means that the crosslinking ratio is relatively weak; however, the stability of the material (in terms of aspect properties and sorption capacities at re-use, see below) sounds poorly affected by the weak crosslinking ratio. This also means that the potential release of formaldehyde will be minimized (in terms of environmental impact). In addition, the advantage of low crosslinking (polymerization degree) consists of enhanced swelling and lower steric hindrance (for improved diffusion properties). The TGA analysis showed that magnetite content was around 34 %; this is consistent with the levels reported in many studies for maintaining efficient magnetic properties without affecting excessively the sorption properties (by direct decrease of the density of reactive groups in the composite material).

3.2. Sorption studies

3.2.1. Effect of pH

The sorption capacity increases with the pH (Fig. 2). Under selected experimental conditions, the sorption capacity is negligible at pH_{eq} ≈1.2, especially for experiments performed in dark and visible light environment below 0.04 mmol U g^{-1}, while submitted to UV irradiation, the sorption capacity slightly increases up to 0.09 mmol U g^{-1}. It is noteworthy that the irradiation mode systematically increases the binding of uranyl ions according to: UV ≫ Vis > Dark. Sorption capacity increases up to a plateau reached at pH_{eq} 4.5; the sorption stabilizes up to pH_{eq}: 5–5.2. The pH_{PZC} values stand between 7.28 and 7.85; meaning that the sorbent surface is systematically positively charged. The competition of protons (and the charge density) decreases with increasing the pH; making the sorbent surface progressively more favorable for uranium binding. It is noteworthy that the type of light exposure poorly affects the pH-edge profiles: the differences in pH_{PZC} do not significantly change the pH range of sorption; the main difference consists of the progressive shift toward higher sorption capacity when the conditions of light exposure become more drastic.

Fig. S9a shows the logarithm plot of the distribution ratio ($D = q_{eq}/C_{eq}$, L g^{-1}) *vs* equilibrium pH for U(VI) sorption under different irradiation modes. For systems driven by ion exchange mechanisms, the slope of the plot may be correlated with the stoichiometric proton-exchange ratio. In the case of dark and visible light exposure, the slope tends to the same value (i.e., 0.63–0.64), lower than the value reached for UV irradiation (i.e., 0.74). These intermediary values state that the binding mechanism is not simply involving proton exchange; metal binding occurs through chelation mechanism.

After U(VI) sorption, the pH slightly increases by less than 0.3 unit until pH 4 for the three modes of light exposure (Fig. S9b). At pH 5, the UV light contributes to decrease the amplitude of pH variation (actually initial pH 5.02 ± 0.01 decreased to 4.93 ± 0.05, contrary to other irradiation modes). The slight pH increase means that the balance between proton binding and proton release due to uranyl binding is more favorable to the accumulation of protons. On the other hand, at pH 5 the formation of hydrolyzed species (and colloids, Fig. S10) consumes hydroxide ions and induces pH decrease, which is enhanced in the case of exposure to UV. This is another evidence of the singularities brought by UV irradiation on U(VI) binding.

3.2.2. Uptake kinetics

The uptake kinetics may be controlled by resistance to diffusion (bulk, film, and intraparticle diffusions) and by the proper reaction rate. Providing a sufficient agitation to avoid sorbent settling, and to enhance the homogeneity of the solution allows neglecting the resistance to bulk diffusion and reducing the effect of the resistance to film diffusion (to the first minutes of contact). Under selected experimental conditions, the equilibrium is reached in 60 min (for tests performed under visible and UV lights) and slightly increases to 90 min for experiments performed in the dark (Fig. 3). These relatively fast kinetic profiles may be explained by the thickness of sorbent particles (1–7 μm): the short diffusion path allows reaching the saturation of the sorbent in 60–90 min. However, taking into account the micron-size of the sorbent, ones would expect faster equilibrium; this probably means that the resistance to intraparticle diffusion plays a role in the control of overall kinetics. Consistently with the observations collected from the study of pH effect, the sorption decreases according UV > Visible > Dark experiments (reciprocal to the increasing trends for residual concentrations). With UV irradiation, uranyl is almost completely recovered from the solution: the sorption yields up to 96.5 %. Another useful information can be extracted from kinetic curves: the initial slope of the decay curves is comparable for UV and visible irradiation conditions, contrary to experiments performed in the dark (substantial decrease of the initial slope).

The fitting of kinetic curves with the pseudo-first (PFORE), pseudo-second order rate (PSORE) and the resistance to intraparticle diffusion (RIDE, or Crank equation) is summarized in Table 1. The values of both R^2 and AIC show that the PFORE is more appropriate than other equations for modeling the kinetics. The calculated sorption capacities at equilibrium systematically overestimate by 5 % the experimental values (i.e., much less than the values found for PSORE model). The changes in the initial slope of the curves with the irradiation mode are consistent with the apparent rate coefficient (i.e., k_1, min^{-1}): UV ($6.48–6.78\times10^{-2}$) > Vis ($5.19–5.55\times10^{-2}$) > Dark ($3.49–3.24\times10^{-2}$). Therefore, the light exposure affects both the equilibrium performance and the kinetics. Since the mode of irradiation is not suspected to affect the diffusion properties of the sorbent, it sounds probable that its effect is due to (a) the change in diffusing metal species or (b) the change in the proper reaction rate (both associated with partial U(VI) reduction). These effects may be completed by the impact of photoreduction.

The simplified model of resistance to intraparticle diffusion poorly fits experimental profiles (not shown but demonstrated by low R^2 and AIC values, in Table 1). However, the model can be used for evaluating the order of magnitude of the effective diffusivity coefficient (i.e., D_e), in the range $1–5\times10^{-14}$ m^2 min^{-1}; which is several orders of magnitude lower than the free diffusivity of uranyl ions in water (i.e., 4.56×10^{-8} m^2 min^{-1}, [62]). This is another proof that the resistance to intraparticle

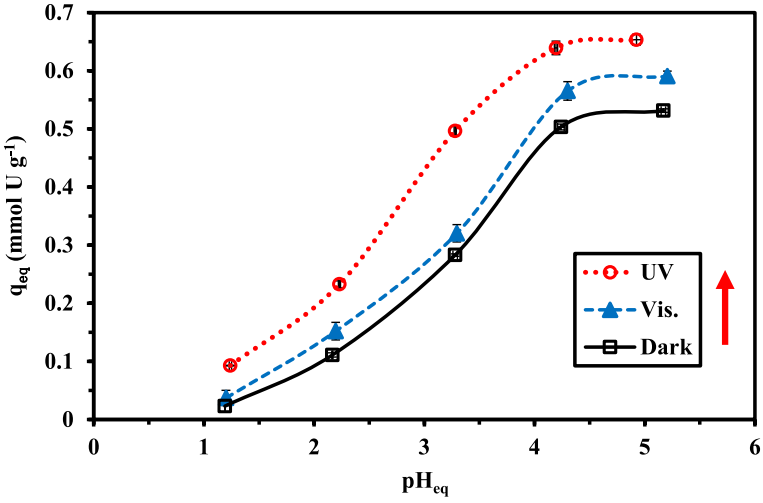

Fig. 2. Effect of equilibrium pH on U(VI) sorption capacity under different modes of light exposure (dark, visible light, and UV light) (C_0: 0.214 mmol U L^{-1}; Sorbent dose, SD: 0.667 g L^{-1}; time: 48 h; T: 20 ± 1 °C; average of two duplicates and standard deviation).

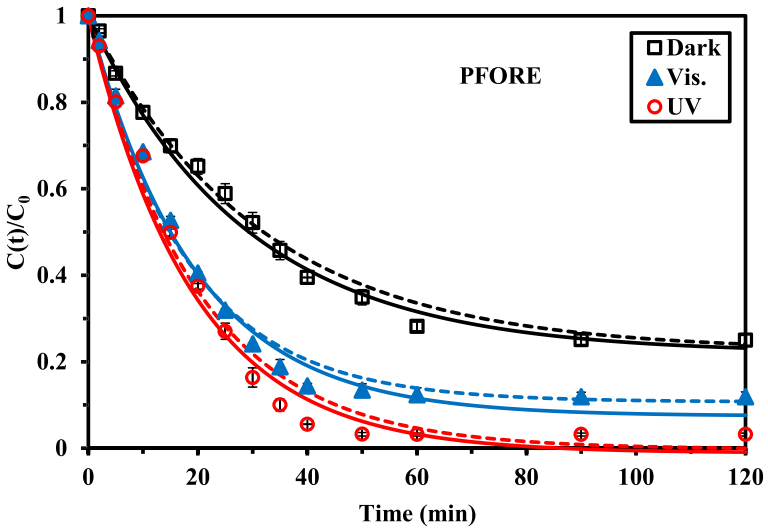

Fig. 3. U(VI) uptake kinetics under different modes of light exposure (dark, visible light, and UV light) – Modeling with the PFORE (solid lines) (C_0: 0.439 mmol U L^{-1}; Sorbent dose, SD: 0.667 g L^{-1}; T: 20 ± 1 °C; v: 210 rpm; average of two duplicates and standard deviation).

Table 1
Modeling of uptake kinetics for U(VI) sorption using M−GANS, for different light exposures.

Model	Parameter	Light exposure					
		Dark		Visible light		UV light	
		D1	D2	V1	V2	UV1	UV2
Experimental	$q_{eq,exp.}$	0.488	0.499	0.572	0.587	0.623	0.651
PFORE	$q_{eq,1}$	0.500	0.524	0.593	0.604	0.648	0.678
	$k_1 \times 10^2$	3.49	3.24	5.19	5.55	6.48	6.78
	R^2	0.996	0.986	0.990	0.993	0.986	0.988
	AIC	−123	−101	−97	−104	−91	−94
PSORE	$q_{eq,2}$	0.607	0.645	0.695	0.701	0.757	0.794
	$k_2 \times 10^2$	6.15	5.16	8.77	9.62	8.22	7.46
	R^2	0.986	0.968	0.960	0.966	0.955	0.959
	AIC	−105	−91	−80	−84	−76	−78
RIDE	$D_e \times 10^{14}$	3.39	3.51	2.73	3.56	0.88	1.01
	R^2	0.980	0.959	0.960	0.962	0.962	0.958
	AIC	−91	−82	−72	−75	−64	−41

Units: q, mmol U g^{-1}; k_1, min^{-1}; k_2, L $mmol^{-1}$ min^{-1}; D_e, m^2 min^{-1} (duplicate series).

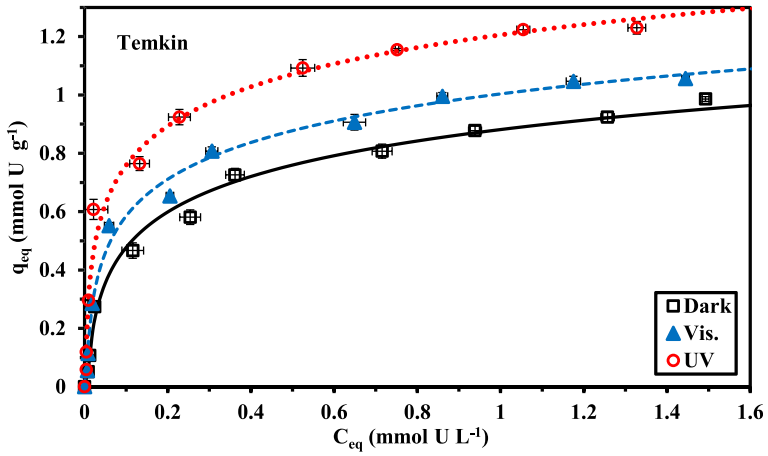

Fig. 4. U(VI) sorption isotherms at pH_0 5 using M−GANS under different modes of light exposure – Modeling with Temkin equation (C_0: 0.042–2.19 mmol U L^{-1}; SD: 0.666 g L^{-1}; time: 48 h; T: 20 ± 1 °C; v: 210 rpm; average of two duplicates and standard deviation).

diffusion contributes to the control of uranyl binding kinetics. Considering the textural properties of the sorbent (Section 3.1.1.), the porosity of the material (pore size in the range (431–583) is much larger than the ionic size of hydrated uranyl ion (i.e., 1.08 for $UO_2(H_2O)_5^{2+}$, [63]). The possible formation of polynuclear species (Fig. S10) may affect the resulting ionic size of the hydrolyzed forms and their diffusion but not enough for restricting the access to sorption sites. However, the drop in diffusivity coefficient confirms the relevant contribution of the resistance to intraparticle diffusion to kinetic control.

3.2.3. Sorption isotherms

The sorption isotherms are also affected by the mode of light exposure (Fig. 4). Consistently with previous observations, when the experiments are performed under light conditions (visible and UV) the sorption of uranyl progressively increases. Herein, both the maximum sorption capacity and the initial slope of the isotherm curves (associated with the affinity coefficient of the sorbent for metal ions) increase. It is noteworthy that even with a residual U(VI) concentration of 1.3–1.5 mmol U L^{-1}, the saturation plateau is not observed (especially for experiments performed in the dark). This observation may explain that the Langmuir equation (Table S2, Fig. S11), which suggest an asymptotic trend, does not give good fitting of experimental profiles (Table 2). The Langmuir equation supposes the sorption to occur as a monolayer without interactions between sorbed species and with homogeneous distribution of sorption energies. The Sips equation combines the mechanistic Langmuir equation with the empirical Freundlich equation (which assumes possible heterogeneities in sorption sites and sorption energies, with possible interactions between sorbed molecules). Adding a third-adjustable parameter in the model improves the quality of the fit (at the expense of loss in physical significance). The Dubinin-Radushkevich model initially developed for gas-solid porous systems has been extrapolated to liquid-solid systems [64]. In the gas-solid systems, the application of the D-R model counts on the filling of space volume in microporous sorbents (rather than the layer-covering hypothesis for alternate models). Herein, the statistical parameters (both R^2 and AIC) confirm that the model is not appropriate for fitting experimental data. The Langmuir Dual Site model accounts for sorption process involving two different reactive groups; this is precisely the case with M−GANS (amino and sulfonic groups). The dual equation improves the quality of the fits of experimental profiles (Table 2, Fig. S11b); however, the Temkin equation (represented by solid lines in Fig. 4) gives the best correlation in modeling isotherm profiles [65] (Table 2, and comparing Fig. 4 and Fig. S11). The Temkin equation assumes that the heat of adsorption linearly decreases with the coverage of the reactive surface [66]. It is noteworthy that the Temkin equilibrium constant (i.e., A_T) significantly increases with light exposure from 151 to 250 L $mmol^{-1}$ for dark and visible light conditions and up to 500 L $mmol^{-1}$ under UV irradiation. On the other side, the b_T constant (which is the Temkin constant related to heat of adsorption) slightly decreases with drastic exposure conditions. This is confirmed by the decrease of the Temkin energy parameter (i.e., E_T) that decreases according 13.97>12.59>10.03 kJ mol^{-1}. The UV irradiation significantly decreases the heat of sorption required for uranyl binding.

Table 2
Modeling of U(VI) sorption isotherm using M− GANS, for different light exposures (parameters calculated for cumulated duplicated series).

Model	Parameter	Unit	Light exposure		
			Dark	Visible light	UV light
Experimental	$q_{m,exp.}$	mmol g^{-1}	0.994	1.065	1.252
Langmuir	$q_{m,L}$	mmol g^{-1}	1.011	1.047	1.181
	b_L	L $mmol^{-1}$	7.27	14.5	28.4
	R^2	–	0.978	0.962	0.948
	AIC	–	−119	−104	−90
Freundlich	k_F	(mmol g^{-1})/(mmol L^{-1})^{nF}	0.892	1.02	1.23
	n_F	–	2.89	3.25	3.61
	R^2	–	0.968	0.947	0.935
	AIC	–	−111	−97	−86
Sips	$q_{m,S}$	mmol g^{-1}	1.246	1.259	1.437
	b_S	(mmol L^{-1})^{nS}	2.541	3.923	4.892
	n_S	–	1.45	1.46	1.57
	R^2	–	0.987	0.974	0.965
	AIC	–	−129	−110	−96
Temkin	A_T	L $mmol^{-1}$	151.5	249.8	499.7
	b_T	kJ kg^{-1} mol^{-2}	13.89	13.41	12.56
	E_T	kJ mol^{-1}	13.97	12.59	10.03
	R^2	–	0.990	0.984	0.975
	AIC	–	−138	−123	−106
D-R	$q_{m,DR}$	mmol g^{-1}	0.929	1.025	1.202
	E_{DR}	kJ mol^{-1}	3.98	8.15	9.36
	R^2	–	0.972	0.966	0.959
	AIC	–	−115	−107	−96
Langmuir dual site	$q_{m,L1}$	mmol g^{-1}	0.575	0.703	0.791
	b_{L1}	L $mmol^{-1}$	21.9	32.75	64.23
	$q_{m,L2}$	mmol g^{-1}	0.772	0.725	0.717
	b_{L2}	L $mmol^{-1}$	0.785	0.793	1.43
	R^2	–	0.990	0.982	0.973
	AIC	–	−131	−113	−98

Table S6 reports the main characteristics of U(VI) sorption onto a wide diversity of sorbents (recently reported in the literature). Some materials show outstanding sorption performances such as diethylenetriamine functionalized MCM-41 sorbent [67] (with maximum sorption capacity up to 4 times the q_m value reported for M−GANS), porous Cu-based MOF [68], amidoximated graphene oxide derivative [69], or zeolitic imidazolate composite [70]. However, M−GANS sorbent represents a good compromise in terms of sorption capacities, and kinetics.

3.2.4. Sorption mechanism

Scheme 2a summarizes the interactions modes between uranyl ions and the reactive groups hold on M−GANS sorbent (i.e., amine groups inter- and intra-chain or cooperatively with sulfonate groups). This mechanism, which is active for the different modes of light exposure, is completed by secondary mechanism of uranium reduction. These reduction mechanisms may take place both on the magnetite core and composite sorbent (through direct mechanism [13,39,71,72]), or by photo-activation [42,73,74]). In addition, to the proper reaction of uranyl ions with functional groups (i.e., amine and sulfonic reactive sites), under irradiation several mechanisms may be involved to reduce U(VI) to U(IV) (which readily precipitates in situ). These photocatalyzed reduction mechanisms may involve not only the direct transfer of electrons at the surface of magnetite but also from the aromatic ring and reactive moieties from ANS (which shows electron withdrawing characteristics). These electrons participate in the reduction of U(VI) to U (IV) [73], which locally precipitate. The contribution of photoreduction phenomena is described in Scheme 2b.

The suspected mechanism of reduction was confirmed by XPS analysis. Fig. S12 compares the core-level spectra for U 4f signal for M−GANS loaded with uranyl under visible and UV irradiation modes. The differences in the profiles clearly demonstrate that the chemical state of uranium is strongly impacted by the exposure to UV light. Indeed, for the sample loaded under visible light three bands can be identified with BEs close to 381.8 eV and 392.7 eV for U $4f_{7/2}$ and U $4f_{5/2}$, respectively, with a complementary band at 386.8 eV for satellite band of U(VI) (Table S7). On the opposite hand, under UV irradiation, the atomic percentages are significantly changed and two new bands are identified at 380.3 eV and 391.2 eV, which correspond to U $4f_{7/2}$ and U

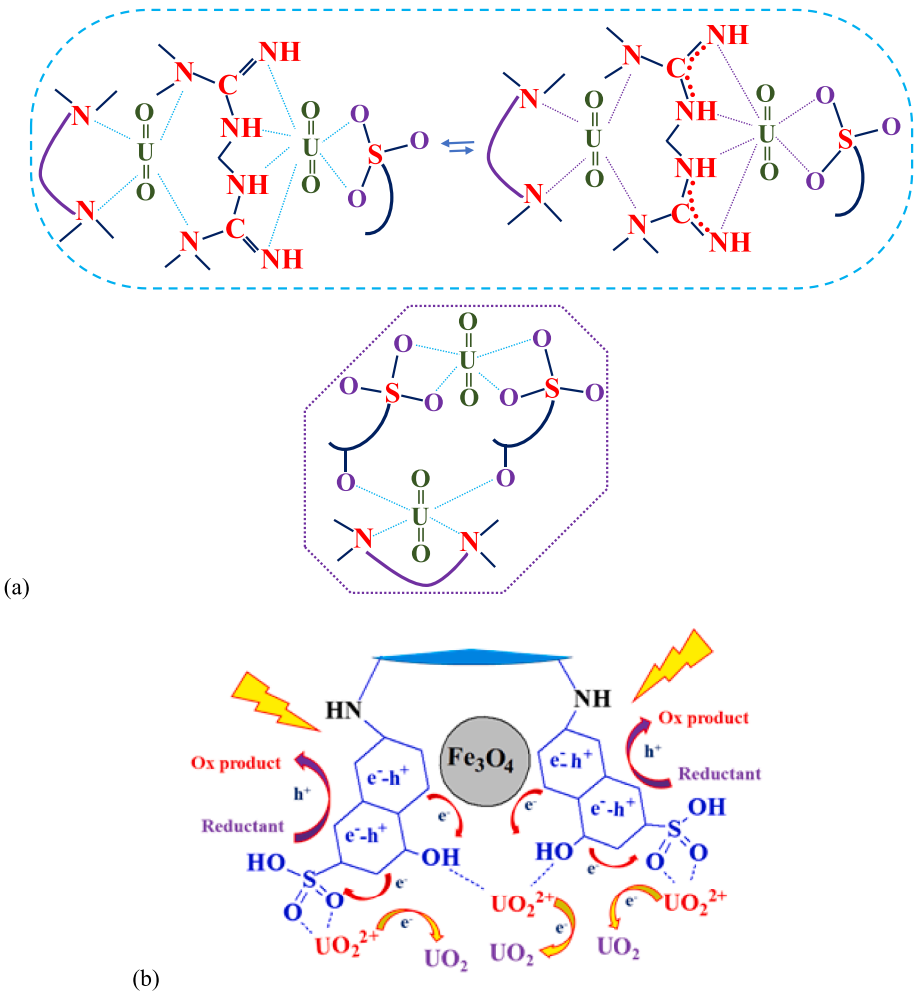

Scheme 2. Tentative mechanisms for the sorption of U(VI) onto the reactive groups at the surface of M−GANS sorbent (a) and contribution of photoreduction phenomena on uranium sorption (b).

$4f_{5/2}$ in reduced oxidation state, respectively [75,76]. The reduced uranium state may correspond to U(IV) and/or U(V) forms [75,77–79].

The UV-irradiation excites Fe_3O_4 surface through photonic energy (*hv*), leading to the release of electrons and formation of electron-lone pairs (h^+ e^-) (Eq. (1a)). The electrons are transferred at the surface of magnetite micro-particles where take place the redox reactions. The hole h^+ interacts with hydroxide ions (OH^-) or water molecules (H_2O) to form hydroxyl radicals ($^{\bullet}OH$) and H^+ (Eq. (1b)), which are highly reactive for uranyl reduction to U(V) (Eq. (1c)) followed by disproportionation into U(VI) and U(IV) species [80] (Eq. (1d)). In addition, electron may activate dissolved oxygen to form superoxide radicals (i.e., $\bullet O_2^-$, Eq. (1e)), which are also highly reactive with uranyl ions to be reduced into U(IV) (Eq. (1f))[81].

$$Fe_3O_4 \xrightarrow{hv} h^+ + e^- \quad (1a)$$

$$h^+ + H_2O \text{ or } OH^- \rightarrow {}^{\cdot}OH + H^+ \quad (1b)$$

$$UO_2^{2+} + h^+ \rightarrow U(V) \quad (1c)$$

$$2\,U(V) \rightarrow UO_2^{2+} + U(IV) \quad (1d)$$

$$O_2 + e \rightarrow {}^{\cdot}O_2^- \quad (1e)$$

$$UO_2^{2+} + 2e^-/\ {}^{\cdot}O_2^- \rightarrow UO_2 \text{ or } O_2 \quad (1f)$$

The propensity of uranyl ions to be photoreduced in the presence of glucosamine and chitosan (aminopolysaccharide) was characterized by the measurement of the difference of potential between two reactors exposed to different light conditions and under different mode of gas sweep (air *vs* nitrogen; i.e., with different oxidative conditions) [41]. Under oxidative conditions (air sweep) and without light exposure, uranyl remains bond onto chitosan without change in color and without difference of potential between the reactors. On the opposite hand, with nitrogen atmosphere and light exposure, the reduction of uranyl in solution and/or at the surface of the sorbent can be proved by color change and difference of potential. Herein, the presence of numerous nitrogen-based (amine) groups contributes to enhance uranyl reduction to U(V) or U(IV). The effect of photoactivation increases while using UV instead of visible light exposure; therefore, the reduction effect is improved, which, in turn, explains the higher sorption performances recorded with UV exposure (compared with visible light irradiation, and even more for experiments performed in the dark).

3.2.5. *Sorption selectivity*

Another criterion for evaluating the potential of new sorbent concerns the efficiency of the material for the selective separation of metal ions. Herein, the sorption properties of M−GANS are investigated at different pH values for the recovery of U(VI) in presence of equimolar concentrations of competitor elements, including Na, Ca, Mg, Fe, Al, Zn and Si (as representatives of the metal ions and metalloid that can be found in the leachate of ores). The experiments are systematically performed in the dark, under visible, and UV light exposures to evaluate the

effect of irradiation on the sorption of individual metals (and more specifically their impact on competition effects). The selectivity coefficient, $SC_{U/Metal}$, is defined as the ratio of distribution ratios (D coefficient) and:

$$SC_{U/Metal} = \frac{D_U}{D_{Metal}} = \frac{q_{eq,U} \times C_{eq,Metal}}{C_{eq,U} \times q_{eq,Metal}} \quad (2)$$

Fig. 5 compares the SC values for the different systems (competitor metal/metalloid, light mode, and pH). First, the highest SC values are systematically reached for the highest pH values (i.e., pH_0: 4–5). The SC values at the optimum pH values can be ranked according:

Dark: Ca(II)≈Si(IV) > Mg(II) > Zn(II)≫Na(I) > Fe(III) > Al(III).

Visible light: Si(IV)≫Ca(II) > Zn(II) > Na(I) > Mg(II) > Fe(III) > Al(III).

UV light: Si(IV)≫Ca(II)≫Na(I) > Fe(III) > Mg(II) > Zn(II) > Al(III).

Though some general trends can be highlighted (such as higher selectivity against Si and Ca; lower selectivity against Fe(III) and Al(III)), some alterations can be identified in the ranking when the mode of exposure changes. Fig. S13 highlights these effects while comparing the changes in the relative variation of selectivity coefficient (compared with dark conditions). In most cases, the UV light brings a significant enhancement in U selectivity; especially for Al(III), Na(I), and Fe(III). On the opposite hand, under visible light, the selectivity tends to decrease (except against Al(III), leading to lower enhancement than under UV irradiation). The differential effects of light exposure on the selectivity coefficients may probably be explained by the sensitivity of competitor ions to partial photoreduction. Li et al. [75] designed a very efficient photoactive metal-organic framework that shows considerable power of extraction of uranium in the presence of ligand. They observed that the presence of non-redox-active metal ions hardly affected U(VI) removal, while Fe(III) significantly decreased uranium removal by depletion of reductive mechanisms (indeed, Fe(III) consumed large quantities of photoelectrons for being reduced). In the application of very active photosensitized materials (Ti^{3+}-doped TiO_2 material) for the adsorption-photocatalysis of U(VI), Wang et al. [69] reported that the presence of competitor metals slightly reduced the sorption capacity of U(VI) and weakly reduced the efficiency of the photo-reduction of uranyl. On the opposite hand, the sorption of the competitor metals was hardly affected by irradiation. Contrary to the current results where the selectivity for U(VI) increases with irradiation, Wang et al. [69] reported a relatively weaker differential between the sorption capacities of U(VI) and competitor metal cations when exposed to visible irradiation.

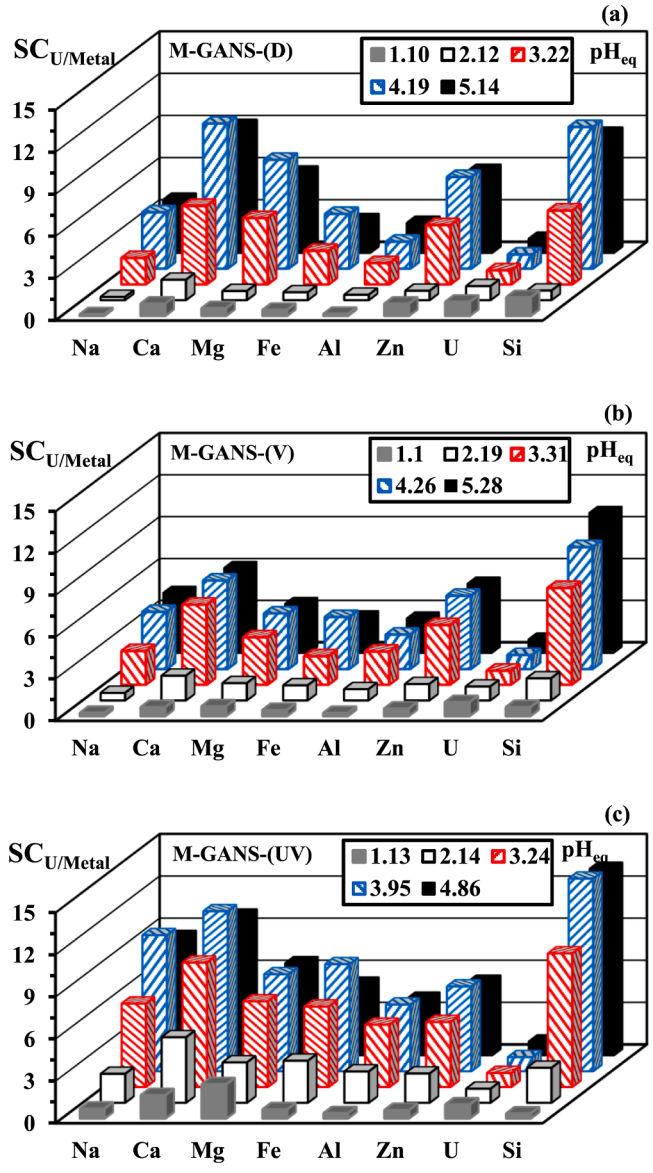

Fig. 5. Effect of pH and mode of light irradiation (a: dark; b: visible; c: UV) on the selectivity coefficient $SC_{U/Metal}$ – Sorption from multi-component equimolar solutions (SD: 1.6 g L^{-1}; equimolar solutions, C_0: 1 mmol L^{-1}; T: 20 ± 1 °C; v: 195 ± 5 rpm; time: 24 h; $SC_{U/U} = 1$, as "internal" reference).

Fig. S14 plots the sorption capacities of individual metals (from multi-component equimolar solutions) at pH_0 5 against covalent index ($X_m^2 \times r$) and ionic index (z^2/r) (where X_m is the Pauling electronegativity, z is the ionic charge of the ion, and r the hydrated radius of the ion). Whatever the criterion (i.e., covalent *vs* ionic index), the sorption capacity for U(VI) appears strongly dispersed compared to the general trend followed by the other metal ions (sorption capacity about 2 times over the expected value from the linear trend). This is another proof that the sorbent demonstrates a remarkable and specific reactivity for U(VI) compared with other competitor ions. Another information resulting from Fig. S14 concerns the "quality" of the correlation between the sorption capacities of metal ions and their covalent or ionic index (out of U(VI) case). Regardless of the light exposure mode, the correlation is slightly better for sorption capacities plotted *vs* the ionic index (Fig. S14d–f) than when plotted against the covalent index (Fig. S14a–c). However, the differences in the correlations are probably not enough marked for assigning the sorption mechanisms to ion-exchange instead of chelation mechanism, despite the effect of protonation of reactive groups on the sorption efficiency. The higher selectivity of M−GANS for U(VI) is probably associated with the favorable steric arrangement of reactive groups (sulfonic and amine) for chelating uranyl linear species.

3.2.6. *Uranium desorption and sorbent recycling*

The sensitivity of U(VI) sorption with pH is a strong incentive to use acidic solutions for the elution of bound metal. The coating of magnetic nanoparticles contributes to preserve their stability. However, concentrated acid solutions could involve partial dissolving of magnetite. For these reasons, metal desorption was investigated using 0.3 M HCl solutions, as a compromise between elution efficiency and stability of the material. Fig. S15 compares the kinetics of U(VI) desorption from metal-loaded sorbents (samples being collected from uptake kinetics under dark, visible light and UV light exposure). The desorption steps were performed under the same conditions of light exposure as those used for preparing specific uranium-loaded samples. For the three sorbents, uranium can be completely desorbed with the acidic solution. Despite the slightly higher metal content in loaded-sorbent processed under UV light, uranium desorption decreases according the series: UV light > visible light > dark conditions. Indeed, the full desorption times correspond to 20 min, 30 min, and 40 min, respectively. These results tend to show that the partial reduction of U(VI), which may occur under UV light, enhances the kinetics of desorption. It is noteworthy that even the

visible light is slightly less favorable than UV light, it shows closer curve from UV light compared with dark conditions.

Hydrochloric acid solution (0.3 M) was used for testing the recycling of the sorbent. Between each individual step water rinsing with deionized water was carried out to neutralize the background environment (of the sorption and desorption steps). Table 3 summarizes the U(VI) sorption and desorption performances for five successive cycles. The desorption efficiency maintains at 99 % (and higher) over the 5 cycles. Desorption performance using 0.3 M HCl solutions is remarkably stable. On the other hand, uranyl sorption progressively decreases while recycling the sorbent. However, the loss in sorption efficiency (under selected experimental conditions) remains relatively limited: 4.3 % under dark conditions, but only 2.1 % under visible light and even lower at 1.4 % under UV light. M− GANS shows outstanding stability at recycling. This conclusion is consistent with the limited impact of sorbent recycling on FTIR spectra (Fig. S6).

3.3. Application to uranium recovery from ore

3.3.1. Pre-treatment of ore

The acid leaching produces a solution containing huge amounts of aluminum and iron (leaching efficiency reaches 22.2 % and 24.9 %, respectively); the process is also highly efficient for extracting trace elements such as uranium (96.7 %), copper (95.6 %), cobalt (88.3 %), REEs (85.4 %), chromium (81.6 %), cadmium (78.0 %), zinc (70.3 %), lead (66.3 %), nickel (65.3 %), or vanadium (56.8 %) (Tables S8 and S9). Table S9 reports the relevant concentrations of selected metals (and Si metalloid) in the leachate: Al(III) and Fe(III) concentrations range around 12 g/L, together with Na(I) (i.e., ≈10 g/L) they represent the major elements in the leachate, while U(VI) concentration counts for 168 mg U L^{-1}. The pre-treatment of this leachate by sorption onto Amberlite IRA-400 ion-exchange resin hardly affects the concentration range of major elements, while about 86 % of uranium is retained on the resin (for the other heavy metals and REEs, the removal efficiency ranges between 12 % for Ni(II) and 68 % for Cu(II)). The outlet solution is pre-treated by precipitation at pH 5 for the removal of the huge excess of iron and aluminum. The series of treatments allows reducing aluminum and iron concentration by 98 % and 99 % respectively; their residual concentrations (i.e., 206 mg Al L^{-1} and 122 mg Fe L^{-1}) are compatible with the conditions of application of M− GANS (limiting competition effects). The effluent used for testing M− GANS sorption at different pH values (with either visible or UV light exposure) contains 18.3 mg U L^{-1} and numerous alkali, alkali-earth, and heavy metals (as appearing in Table S9). Apart Na(I) (i.e., 9.5 g Na L^{-1}), major competitor metal ions are Ca(II), Mn(II), Mg(II), Al(III), K(I), Cu(II), Fe(III), Zn(II), and Co(II). This complex composition allows completing the study of selectivity issues for uranium recovery with M− GANS.

Table 3
Sorbent recycling for U(VI) recovery using M− GANS (loaded under different modes of light exposure) – Sorption (SE, %) and desorption (DE, %) efficiencies.

Exposure	Dark		Visible Light		UV Light	
Cycle	SE	DE	SE	DE	SE	DE
1	78.2 ± 0.7	100.1 ± 0.2	87.8 ± 0.8	99.8 ± 0.3	93.4 ± 1.4	99.8 ± 0.4
2	77.6 ± 0.4	100.3 ± 0.9	87.2 ± 0.3	99.7 ± 0.8	93.0 ± 1.6	99.7 ± 0.3
3	76.5 ± 0.2	100.5 ± 1.5	86.7 ± 0.5	100.0 ± 0.7	92.7 ± 1.6	99.8 ± 0.1
4	75.8 ± 0.6	100.6 ± 0.5	86.2 ± 0.3	99.9 ± 0.1	92.3 ± 1.4	100.0 ± 0.0
5	74.9 ± 0.8	98.9 ± 0.8	86.0 ± 0.3	99.8 ± 0.3	92.1 ± 1.4	99.9 ± 0.2
Loss in sorption $5^{th}/1^{st}$	4.3 %		2.1 %		1.4 %	

3.3.2. Effect of light exposure on the recovery and selective separation of uranium using M−GANS

Fig. S16 compares the $\log_{10}$ plots of the distribution ratio (D, L g^{-1}) *vs* pH_{eq} for selected metal ions under different modes of light exposure (visible and UV lights). The distribution ratio systematically increases with the pH up to 4 before stabilizing (between pH 4 and 5). The highest values are obtained for U(VI) and Fe(III), significantly greater than other grouped metals. In addition, the UV irradiation tends to highlight these differences between U(VI)/Fe(III) and other competitor metals (for this series of metals the distribution ratio is weakly affected by UV irradiation *vs* visible light).

In terms of distribution ratio, the metals in the effluent can systematically be ranked according the series (independently of pH and irradiation mode):

$$U(VI) \gg Fe(III) \gg Zn(II) \approx Cu(II) > Mg(II) > Al(III) > Ca(II) > Mn(II)$$

With visible light, the greatest difference in the distribution ratio between U and competitor metals (in $\log_{10}$ units) is reached at pH_0 5 (i.e., pH_{eq}, 4.89), while under UV irradiation the pH of highest differences is shifted to pH_0 4 (i.e., pH_{eq}, 3.89). Based on this information, it is possible anticipating that UV irradiation will enhance the selectivity of M−GANS for U(VI) recovery against other competitor metals at pH_0 5. Fig. 6 that shows the effect of equilibrium pH on the selectivity coefficient $SC_{U/metal}$, under visible and UV light exposure confirm this. The UV irradiation systematically increases twice (or more) the preference of the sorbent for uranium over competitor metals, when compared with visible light. For visible light system, the optimum pH for uranium preference change with the competitor metal: pH_{eq} 3.27 for Mg(II) and Cu(II), and pH 4.89 for the others. In the case of UV irradiation, pH_{eq} 3.89 is preferred (except for Ca(II) where the values are close between pH_{eq} 3.89 and 4.81). The interpretation of sorbent preference is made complex by the differences in the relative concentrations of uranium and competitor metals (contrary to the tests performed at equimolar concentrations in Section 3.2.5.). The UV light considerably increases the preference for uranium even in a complex solution as the tested effluent. Factually, the $SC_{U/metal}$, under the most favorable conditions, follows the trend:

$$U(VI) \gg Fe(III) \gg Zn(II) \approx Cu(II) \gg Ca(II) \approx Mg(II) \approx Al(III) \gg Mn(II).$$

This ranking is roughly consistent with the observations reported in the study of selectivity, with effects modulated by the differences in relative concentrations (and molar excess in the feed solution). It is noteworthy that the results obtained on pre-treated leachate cannot be directly compared with the data collected from tests on synthetic solutions. Indeed, while uranyl nitrate salt was used for preparing synthetic solutions, in the case of pre-treated leachates the metal is present as uranyl sulfate species (i.e., $UO_2(SO_4)_2^{2-}$ and/or $UO_2(SO_4)_3^{4-}$, [14]). Anionic uranyl species are supposed to be bound onto protonated amine groups, while sulfonate groups will be less reactive.

3.3.3. Metal elution and uranium recovery by precipitative reduction

For the specific study of desorption performance with sorbent loaded with pre-treated leachates, the batch sorption allows decreasing the concentration of the solution from 18.2 mg U L^{-1} to 3.18 and 1.92 mg U L^{-1}, under visible and UV irradiation, respectively. The sorption efficiencies reach 82.5 % and 89.5 %, respectively and the sorption capacity are 37.6 mg U g^{-1} (i.e., 0.158 mmol U g^{-1}) and 40.7 mg U g^{-1} (i.e., 0.171 mmol U g^{-1}), respectively. Nitric acid solution (1 M) successfully desorbs uranium; the uranium concentrations in the eluates reach 7150 and 7700 mg U L^{-1}, respectively. The desorption efficiencies reach 95.2 % and 94.6 %, respectively.

The valorization of uranium was processed through acid precipitation (at pH 2.5) in the presence of H_2O_2 (in little excess) under the form of $UO_4{\cdot}nH_2O$ [82,83]. Semi quantitative EDX analysis of the water-rinsed precipitate shows that the impurities represent less than 1.6 %

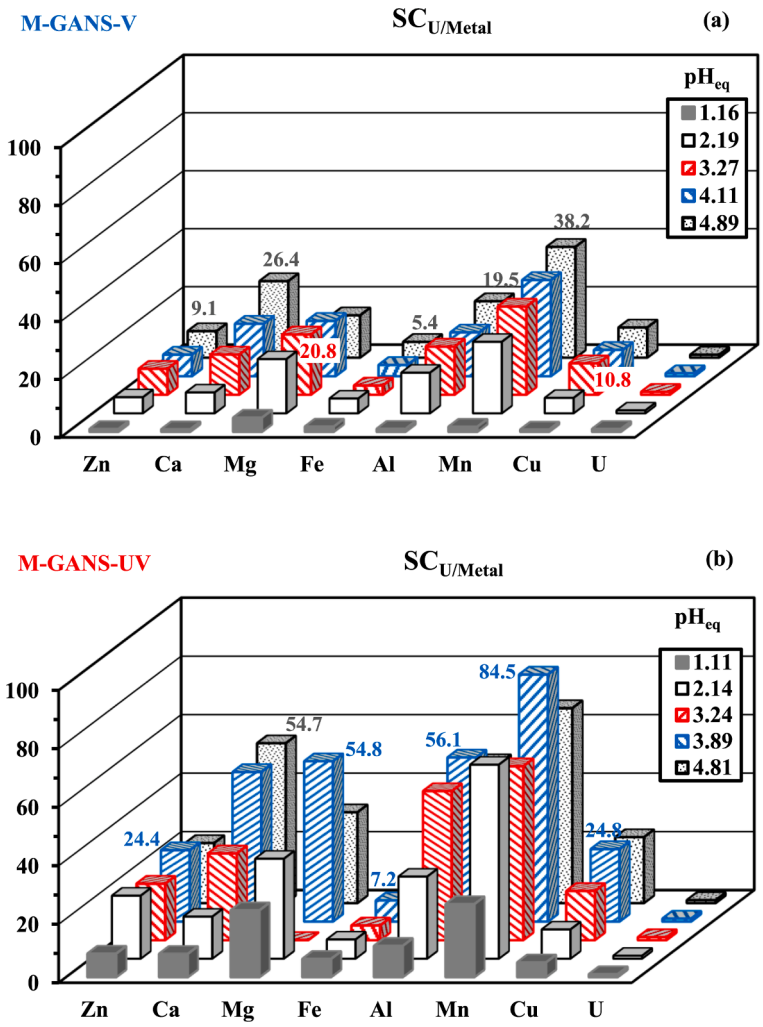

Fig. 6. Effect of pH_{eq} on $SC_{U/metal}$ for the application of M−GANS to pre-treated ore leachate – Effect of Visible (a) and UV light exposure (b) (SD: 4 g L^{-1}; time: 5 h; v: 195 ± 5 rpm; T: 20 ± 1 °C; $SC_{U/U} = 1$, as "internal" reference).

(w/w) in the case of M−GANS loaded under visible light, and less than 1.1 % (w/w) for the case of UV irradiation (Fig. S17). This is consistent with the increased selectivity of the sorbent for U against competitor metal ions under UV exposure. The major contaminants are sodium (0.5–0.3 %), iron (0.7–0.5 %), and calcium (0.3–0.2 %). The UV irradiation brings an additional benefit while producing a higher purity grade for the U precipitate.

4. Conclusions

Magnetic bi-functional sorbent (based on the polycondensation of guanidine with amino hydroxy-naphthalenesulfonic acid derivative in the presence of formaldehyde) reveals an efficient sorbent for U(VI) under mild acidic conditions (i.e., pH 4–5). Exposing the sorption system to light influences uranyl sorption performance both in terms of equilibrium and kinetics. The maximum sorption capacity increases with the "strength" of the mode of irradiation: +7% with visible light and up to +26 % with UV irradiation (compared with dark experiment). The binding proceeds through direct interactions between UO_2^{2+} ions and both amine and sulfonate groups. In addition, the photoactivation of the reactor involves complementary removal of uranium through reduction mechanism (stimulated by both the magnetic micro-particles and the reductive effect of amine groups, as confirmed by XPS analysis). Uptake kinetics (which are controlled by the pseudo-first order rate equation) are relatively fast (due to the small size of sorbent particles and their porous characteristics): equilibrium is reached in less than 90 min. Sorption isotherms are fitted by the Temkin equation preferentially to Langmuir, Sips and Dubininn-Radushkevich equations. The sorbent shows remarkable selectivity for U(VI) against conventional competitor metals both with synthetic equimolar solutions and processed ore leachates. It is remarkable that the selectivity is enhanced by UV irradiation (probably associated to a lower impact of photoactivation on the reduction of selected competitor metals). The same benefit of irradiation is also observed in the recycling of the sorbent: desorption efficiency appears independent of the mode of light exposure (maintaining higher than 99 % over five cycles). However, the stability of sorption properties decreases with the recycling more significantly when sorption and desorption are processed in the dark. These results show the sensitivity of sorption mechanisms and performances to light conditions; this may explain (to a certain extent) the variability observed in sorption data when experimental conditions are not perfectly controlled. In addition, assisting uranyl sorption process with optimized irradiation could open possibilities for enhancing the sorption performance of M−GANS.

Uranium was successfully recovered from pre-treated acidic ore leachate. After pre-treatment by sorption on Amberlite IRA-400 ion-exchanger, the leachate was controlled to pH 5 for sorption onto M−GANS sorbent under both visible and UV irradiation. After successful elution (yield ≈95 %), the pH-controlled precipitation (in the presence of hydrogen peroxide) generates a $UO_4{\cdot}nH_2O$ peroxide (with limited impurities).

Declaration of Competing Interest

The authors declare that they have no known competing financial interests or personal relationships that could have appeared to influence the work reported in this paper.

Data availability

Data will be made available on request.

Acknowledgements

Y.W acknowledges the National Natural Science Foundation of China for supporting projects [U1967218, and 11975082].

Appendix A. Supplementary data

Supplementary data to this article can be found online at https://doi.org/10.1016/j.cej.2022.141099.

References

[1] E. Rosenberg, G. Pinson, R. Tsosie, H. Tutu, E. Cukrowska, Uranium remediation by ion exchange and sorption methods: A critical review - various types of solid phase sorbents are studied and evaluated, Johnson Matthey, Technol. Rev. 60 (2016) 59–77.
[2] T. Tatarchuk, A. Shyichuk, I. Mironyuk, M. Naushad, A review on removal of uranium(VI) ions using titanium dioxide based sorbents, J. Mol. Liq. 293 (2019), 111563.
[3] M. Jimenez-Reyes, P.T. Almazan-Sanchez, M. Solache-Rios, Radioactive waste treatments by using zeolites. A short review, J. Environ. Radioact. 233 (2021), 106610.
[4] M.M. Nezhad, A. Semnani, N. Tavakkoli, M. Shirani, Selective and highly efficient removal of uranium from radioactive effluents by activated carbon functionalized with 2-aminobenzoic acid as a new sorbent, J. Environ. Manage. 299 (2021), 113587.
[5] K. Patra, S.A. Ansari, P.K. Mohapatra, Metal-organic frameworks as superior porous adsorbents for radionuclide sequestration: Current status and perspectives, J. Chromatogr. A 1655 (2021), 462491.
[6] L. Huang, R. Liu, J. Yang, Q. Shuai, B. Yuliarto, Y.V. Kaneti, Y. Yamauchi, Nanoarchitectured porous organic polymers and their environmental applications for removal of toxic metal ions, Chem. Eng. J. 408 (2021), 127991.
[7] N. Tang, J. Liang, C. Niu, H. Wang, Y. Luo, W. Xing, S. Ye, C. Liang, H. Guo, J. Guo, et al., Amidoxime-based materials for uranium recovery and removal, J. Mater. Chem. A 8 (2020) 7588–7625.
[8] J.T.M. Amphlett, S. Choi, S.A. Parry, E.M. Moon, C.A. Sharrad, M.D. Ogden, Insights on uranium uptake mechanisms by ion exchange resins with chelating functionalities: Chelation vs. anion exchange, Chem. Eng. J. 392 (2020), 123712.
[9] Z. Wen, K. Huang, Y. Niu, Y. Yao, S. Wang, Z. Cao, H. Zhong, Kinetic study of ultrasonic-assisted uranium adsorption by anion exchange resin, Colloids Surf., A 585 (2020), 124021.
[10] O.E. Roshdy, Removal of uranium, cadmium and iron ions from phosphoric acid solution using amberjet 1200 H resin: an experimental, isotherm and kinetic study, J. Radioanal. Nucl. Chem. 329 (2021) 85–101.
[11] M.H. Taha, Solid-liquid extraction of uranium from industrial phosphoric acid using macroporous cation exchange resins: MTC1600H, MTS9500, and MTS9570, Sep. Sci. Technol. 56 (2021) 1562–1578.
[12] Y. Xie, C. Chen, X. Ren, X. Wang, H. Wang, X. Wang, Emerging natural and tailored materials for uranium-contaminated water treatment and environmental remediation, Prog. Mater Sci. 103 (2019) 180–234.
[13] H. Liao, J. Yu, W. Zhu, M. Kuang, T. Duan, Y. Zhang, X. Lin, X. Luo, J. Zhou, Nano-zero-valent Fe/Ni particles loaded on collagen fibers immobilized by bayberry tannin as an effective reductant for uranyl in aqueous solutions, Appl. Surf. Sci 507 (2020), 145075.
[14] G. Michailidou, I. Koumentakou, E.V. Liakos, M. Lazaridou, D.A. Lambropoulou, D. N. Bikiaris, G.Z. Kyzas, Adsorption of uranium, mercury, and rare earth elements from aqueous solutions onto magnetic chitosan adsorbents: A review, Polymers 13 (2021) 3137.
[15] M.M. Lazar, I.A. Dinu, M.V. Dinu, Synthesis of ethylenediaminetetraacetic acid-functionalized chitosan cryogels as potential sorbents of heavy metal ions, Materiale Plastice 58 (2021) 155–166.
[16] C. Gao, X.L. Wang, Q.D. An, Z.Y. Xiao, S.R. Zhai, Synergistic preparation of modified alginate aerogel with melamine/chitosan for efficiently selective adsorption of lead ions, Carbohydr. Polym. 256 (2021), 117564.
[17] A.M. Atta, Z.H. Abd El Wahab, Z.A. El Shafey, W.I. Zidan, Z.F. Akl, Uranyl ions uptake from aqueous solutions using crosslinked ionic copolymers based on 2-acrylamido-2-methylpropane sulfonic acid copolymers, J. Dispersion Sci. Technol. 31 (2010) 1601–1610.
[18] M.G. Torkabad, A.R. Keshtkar, S.J. Safdari, Comparison of polyethersulfone and polyamide nanofiltration membranes for uranium removal from aqueous solution, Prog. Nucl. Energy 94 (2017) 93–100.
[19] M.O.A. El-Magied, A.S. Dhmees, A.A.M. Abd El-Hamid, E.M. Eldesouky, Uranium extraction by sulfonated mesoporous silica derived from blast furnace slag, J. Nucl. Mater. 509 (2018) 295–304.
[20] A. Syamal, M.M. Singh, Reactive polymers. II. Novel polystyrene-anchored copper (II), nickel(II), cobalt(II), iron(III), zinc(II), cadmium(II), zirconium(IV), molybdenum(V), molybdenum(VI) and uranium(VI) complexes of the chelating resin containing the Schiff base derived from salicylaldehyde and 1-amino-2-naphthol-4-sulphonic acid, React. Polym., 21 (1993) 149-158.
[21] M. Gregusova, B. Docekal, New resin gel for uranium determination by diffusive gradient in thin films technique, Anal. Chim. Acta 684 (2011) 142–146.
[22] K. Sanyal, S. Chappa, N. Pathak, A.K. Pandey, N.L. Misra, Trace element determinations in uranium by total reflection X-Ray fluorescence spectrometry using a newly developed polymer resin for major matrix separation, Spectrochim. Acta, Part B 150 (2018) 18–25.
[23] P.P. Yang, Q. Liu, J.Y. Liu, R.R. Chen, R.M. Li, X.F. Bai, J. Wang, Highly efficient immobilization of uranium(VI) from aqueous solution by phosphonate-functionalized dendritic fibrous nanosilica (DFNS), J. Hazard. Mater. 363 (2019) 248–257.
[24] M.F. Hamza, K.A.M. Salih, A.A.H. Abdel-Rahman, Y.E. Zayed, Y. Wei, J. Liang, E. Guibal, Sulfonic-functionalized algal/PEI beads for scandium, cerium and holmium sorption from aqueous solutions (synthetic and industrial samples), Chem. Eng. J. 403 (2021), 126399.
[25] K.L. Ang, D. Li, A.N. Nikoloski, The effectiveness of ion exchange resins in separating uranium and thorium from rare earth elements in acidic aqueous sulfate media. Part 1. Anionic and cationic resins, Hydrometallurgy 174 (2017) 147–155.
[26] K.L. Ang, D. Li, A.N. Nikoloski, The effectiveness of ion exchange resins in separating uranium and thorium from rare earth elements in acidic aqueous sulfate media. Part 2. Chelating resins, Miner. Eng. 123 (2018) 8–15.
[27] E.P. Horwitz, R. Chiarizia, H. Diamond, R.C. Gatrone, S.D. Alexandratos, A. Q. Trochimczuk, D.W. Crick, Uptake of metal-ions by a new chelating ion-exchange resin. 1. Acid dependencies of actinide ions, Solvent Extr. Ion Exch. 11 (1993) 943–966.
[28] S.D. Alexandratos, X. Zhu, Polymer-supported aminomethylphosphinate as a ligand with a high affinity for U(VI) from phosphoric acid solutions: Combining variables to optimize ligand-ion communication, Solvent Extr. Ion Exch. 34 (2016) 290–295.
[29] D. Ma, J. Wei, Y. Zhao, Y. Chen, S. Tang, The removal of uranium using novel temperature sensitive urea-formaldehyde resin: adsorption and fast regeneration, Sci. Total Environ. 735 (2020), 139399.
[30] Z.-A. Lan, W. Ren, X. Chen, Y. Zhang, X. Wang, Conjugated donor-acceptor polymer photocatalysts with electron-output “tentacles” for efficient hydrogen evolution, Appl. Catal., B 245 (2019) 596–603.
[31] W. Liang, M. Lv, X. Yang, Development of a physics-based model for analyzing formaldehyde emissions from building material under coupling effects of temperature and humidity, Building and Environment 203 (2021), 108078.
[32] T. Zorba, E. Papadopoulou, A. Hatjiissaak, K.M. Paraskevopoulos, K. Chrissafis, Urea-formaldehyde resins characterized by thermal analysis and FTIR method, J. Therm. Anal. Calorim. 92 (2008) 29–33.
[33] M.F. Hamza, A. Gamal, G. Hussein, M.S. Nagar, A.A.H. Abdel-Rahman, Y. Wei, E. Guibal, Uranium(VI) and zirconium(IV) sorption on magnetic chitosan derivatives - effect of different functional groups on separation properties, J. Chem. Technol. Biotechnol. 94 (2019) 3866–3882.
[34] M.F. Hamza, A.A.H. Abdel-Rahman, E. Guibal, Magnetic glutamine-grafted polymer for the sorption of U(VI), Nd(III) and Dy(III), J. Chem. Technol. Biotechnol. 93 (2018) 1790–1806.
[35] A.A. Galhoum, W.H. Eisa, I.-E.-T. El-Sayed, A.A. Tolba, Z.M. Shalaby, S. I. Mohamady, S.S. Muhammad, S.S. Hussien, T. Akashi, E. Guibal, A new route for manufacturing poly(aminophosphonic)-functionalized poly(glycidyl methacrylate)-magnetic nanocomposite - Application to uranium sorption from ore leachate, Environ. Pollut. 264 (2020), 114797.
[36] W.D. Xiao, L.P. Xiao, Y.H. Lv, W.Z. Yin, J. Sanchez, S.R. Zhai, Q.D. An, R.C. Sun, Lignin-derived carbon coated nanoscale zero-valent iron as a novel bifunctional material for efficient removal of Cr(VI) and organic pollutants, Sep. Purif. Technol. 299 (2022), 121689.
[37] Q. Wang, C. Zhu, X. Huang, G. Yang, Abiotic reduction of uranium(VI) with humic acid at mineral surfaces: Competing mechanisms, ligand and substituent effects, and electronic structure and vibrational properties, Environ. Pollut. 254 (2019), 113110.
[38] Y.N. Vodyanitskii, Chemical aspects of uranium behavior in soils: A review, Eurasian Soil Sci. 44 (2011) 862–873.
[39] H. Liao, W. Zhu, T. Duan, Y. Zhang, G. He, Y. Wei, J. Zhou, Beaded segments like bi-metallic nano-zero-valent iron-titanium for the fast and efficient adsorption and reduction of U(VI) in aqueous solutions, Colloids Surf., A 613 (2021), 126080.
[40] L. Xu, D. Zhang, F. Ma, J. Zhang, A. Khayambashi, Y. Cai, L. Chen, C. Xiao, S. Wang, Nano-MOF+ technique for efficient uranyl remediation, ACS Appl. Mater. Interfaces 11 (2019) 21619–21626.
[41] E. Guibal, J. Roussy, P. LeCloirec, Photochemical reaction of uranium with glucosamine, acetylglucosamine and related polymers: Chitin and chitosan, Water Sa 22 (1996) 19–26.
[42] M. Chen, T. Liu, S. Tang, T. Wei, A. Gu, R. Zhang, Y. Liu, H. Wang, Z. Xie, Y. Yuan, et al., Mixed-linker strategy toward enhanced photoreduction-assisted uranium recovery from wastewater and seawater, Chem. Eng. J. 446 (2022), 137264.

[43] R. Massart, Preparation of aqueous magnetic liquids in alkaline and acidic media, IEEE Trans. Magn. 17 (1981) 1247–1249.
[44] Z. Marczenko, M. Balcerzak, Chapter 39 - Rare-earth elements, in: Z. Marczenko, M. Balcerzak (Eds.), Analytical Spectroscopy Library, Elsevier, 2000, pp. 341–349.
[45] M. Bickel, The Davies-Gray titration for the assay of uranium in nuclear materials: A performance study, J. Nucl. Mater. 246 (1997) 30–36.
[46] O. Falyouna, O. Eljamal, I. Maamoun, A. Tahara, Y. Sugihara, Magnetic zeolite synthesis for efficient removal of cesium in a lab-scale continuous treatment system, J. Colloid Interface Sci. 571 (2020) 66–79.
[47] M. Thommes, K. Kaneko, A.V. Neimark, J.P. Olivier, F. Rodriguez-Reinoso, J. Rouquerol, K.S.W. Sing, Physisorption of gases, with special reference to the evaluation of surface area and pore size distribution (IUPAC Technical Report), Pure Appl. Chem. 87 (2015) 1051–1069.
[48] L.-L. Liu, Z.-H. Cui, J.-J. Wang, Z.-H. Xia, L.-J. Duan, Y. Yang, M. Li, T. Li, Pore size distribution characteristics of high rank coal with various grain sizes, ACS Omega 5 (2020) 19785–19795.
[49] K. Petcharoen, A. Sirivat, Synthesis and characterization of magnetite nanoparticles via the chemical co-precipitation method, Mater. Sci. Eng., B 177 (2012) 421–427.
[50] H. Iida, K. Takayanagi, T. Nakanishi, T. Osaka, Synthesis of Fe_3O_4 nanoparticles with various sizes and magnetic properties by controlled hydrolysis, J. Colloid Interface Sci. 314 (2007) 274–280.
[51] A. Ibanescu, M.C. Alexandrica, D. Hritcu, O. Chiscan, M.I. Popa, Magnetite/chitosan composite particles as adsorbents for Reactive Blue 19 dye, Green Mater. 6 (2018) 149–156.
[52] E. Cheraghipour, M. Pakshir, Process optimization and modeling of Pb(II) ions adsorption on chitosan-conjugated magnetite nano-biocomposite using response surface methodology, Chemosphere 260 (2020), 127560.
[53] Y.H. Chen, Thermal properties of nanocrystalline goethite, magnetite, and maghemite, J. Alloys Compd. 553 (2013) 194–198.
[54] H. Javadian, M. Ruiz, T.A. Saleh, A.M. Sastre, Ca-alginate/carboxymethyl chitosan/$Ni_{0.2}Zn_{0.2}F_{2.6}O_4$ magnetic bionanocomposite: Synthesis, characterization and application for single adsorption of Nd^{+3}, Tb^{+3}, and Dy^{+3} rare earth elements from aqueous media, J. Mol. Liq. 306 (2020), 112760.
[55] E. Alver, A.Ü. Metin, F. Brouers, Methylene blue adsorption on magnetic alginate/rice husk bio-composite, Int. J. Biol. Macromol. 154 (2020) 104–113.
[56] Y.W. Cai, C.F. Wu, Z.Y. Liu, L.J. Zhang, L.H. Chen, J.Q. Wang, X.K. Wang, S. T. Yang, S. Wang, Fabrication of a phosphorylated graphene oxide-chitosan composite for highly effective and selective capture of U(VI), Environ. Sci, Nano 4 (2017) 1876–1886.
[57] D. Lin-Vien, N.B. Colthup, W.G. Fateley, J.G. Grasselli, APPENDIX 3 - A Summary of Characteristic Raman and Infrared Frequencies, in: D. Lin-Vien, N.B. Colthup, W. G. Fateley, J.G. Grasselli (Eds.), The Handbook of Infrared and Raman Characteristic Frequencies of Organic Molecules, Academic Press, San Diego, 1991, pp. 477–490.
[58] C. Cao, K. Wu, W. Yuan, Y. Zhang, H. Wang, Synthesis of non-water soluble polymeric guanidine derivatives and application in preparation of antimicrobial regenerated cellulose, Fibers Polym. 18 (2017) 1040–1047.
[59] Z. Yan-Min, Study on naphthalene sulfonic acid formaldehyde condensate by ultraviolet absorption spectrum, J. Phys. Conf. Ser. 1237 (2019), 022107.
[60] H. Yang, X. Guo, R. Chen, Q. Liu, J. Liu, J. Yu, C. Lin, J. Wang, M. Zhang, A hybrid sponge with guanidine and phytic acid enriched surface for integration of antibiofouling and uranium uptake from seawater, Appl. Surf. Sci 525 (2020), 146611.
[61] E. Katoueizadeh, S.M. Zebarjad, K. Janghorban, Investigating the effect of synthesis conditions on the formation of urea–formaldehyde microcapsules, Journal of Materials Research and Technology 8 (2019) 541–552.
[62] Y. Marcus, Ion Properties, Marcel Dekker Inc, New York, NY, 1997, p. 259.
[63] I. Persson, Hydrated metal ions in aqueous solution: How regular are their structures? Pure Appl. Chem. 82 (2010) 1901–1917.
[64] V. Puccia, M.J. Avena, On the use of the Dubinin-Radushkevich equation to distinguish between physical and chemical adsorption at the solid-water interface, Colloid Interface Sci. Commun. 41 (2021), 100376.
[65] K.H. Chu, Revisiting the Temkin isotherm: Dimensional inconsistency and approximate forms, Ind. Eng. Chem. Res. 60 (2021) 13140–13147.
[66] C.S.T. Araujo, I.L.S. Almeida, H.C. Rezende, S. Marcionilio, J.J.L. Leon, T.N. de Matos, Elucidation of mechanism involved in adsorption of Pb(II) onto lobeira fruit (*Solanum lycocarpum*) using Langmuir, Freundlich and Temkin isotherms, Microchem. J. 137 (2018) 348–354.
[67] P. Amesh, K.A. Venkatesan, A.S. Suneesh, N. Samanta, Diethylenetriamine tethered mesoporous silica for the sequestration of uranium from aqueous solution and seawater, J. Environ. Chem. Eng. 8 (2020), 103995.
[68] C. Duan, Y. Zhang, J. Li, L. Kang, Y. Xie, W. Qiao, C. Zhu, H. Luo, Rapid room-temperature preparation of hierarchically porous metal-organic frameworks for efficient uranium removal from aqueous solutions, Nanomaterials 10 (2020) 1539.
[69] Y. Wang, X. Hu, Y. Liu, Y. Li, T. Lan, C. Wang, Y. Liu, D. Yuan, X. Cao, H. He, et al., Assembly of three-dimensional ultralight poly(amidoxime)/graphene oxide nanoribbons aerogel for efficient removal of uranium(VI) from water samples, Sci. Total Environ. 765 (2021), 142686.
[70] Y. Liu, Y. Huo, X. Wang, S. Yu, Y. Ai, Z. Chen, P. Zhang, L. Chen, G. Song, N. S. Alharbi, et al., Impact of metal ions and organic ligands on uranium removal properties by zeolitic imidazolate framework materials, J. Cleaner Prod. 278 (2021), 123216.
[71] B. Gu, L. Liang, M.J. Dickey, X. Yin, S. Dai, Reductive precipitation of uranium(VI) by zero-valent iron, Environ. Sci. Technol. 32 (1998) 3366–3373.
[72] Z.Z. Pan, B. Bartova, T. LaGrange, S.M. Butorin, N.C. Hyatt, M.C. Stennett, K. O. Kvashnina, R. Bernier-Latmani, Nanoscale mechanism of UO_2 formation through uranium reduction by magnetite, Nat. Commun. 11 (2020).
[73] F.T. Yu, Z.Q. Zhu, S.P. Wang, Y.K. Peng, Z.Z. Xu, Y.A. Tao, J.B. Xiong, Q.W. Fan, F. Luo, Tunable perylene-based donor-acceptor conjugated microporous polymer to significantly enhance photocatalytic uranium extraction from seawater, Chem. Eng. J. 412 (2021), 127558.
[74] L. Chen, B. Chen, J.Y. Kang, Z.J. Yan, Y.D. Jin, H.J. Yan, S.Y. Chen, C.Q. Xia, The synthesis of a novel conjugated microporous polymer and application on photocatalytic removal of uranium(VI) from wastewater under visible light, Chem. Eng. J. 431 (2022), 133222.
[75] H. Li, F.W. Zhai, D.X. Gui, X.X. Wang, C.F. Wu, Z. Duo, D. Xing, D. Hong, X.T. Su, D. Juan, et al., Powerful uranium extraction strategy with combined ligand complexation and photocatalytic reduction by postsynthetically modified photoactive metal-organic frameworks, Applied Catalysis B-Environmental 254 (2019) 47–54.
[76] C. Chen, J. Hu, J. Wang, Uranium biosorption by immobilized active yeast cells entrapped in calcium-alginate-PVA-GO-crosslinked gel beads, Radiochim. Acta 108 (2020) 273–286.
[77] T. Gouder, R. Eloirdi, R. Caciuffo, Direct observation of pure pentavalent uranium in U_2O_5 thin films by high resolution photoemission spectroscopy, Sci. Rep. 8 (2018) 8306.
[78] G. Heisbourg, S. Hubert, N. Dacheux, J. Purans, Kinetic and thermodynamic studies of the dissolution of thoria-urania solid solutions, J. Nucl. Mater. 335 (2004) 5–13.
[79] T.B. Scott, G.C. Allen, P.J. Heard, A.C. Lewis, D.F. Lee, The extraction of uranium from groundwaters on iron surfaces, Proc. R. Soc. London, Ser. A, 461 (2005) 1247-1259.
[80] A.J. Elliot, P. Shahsultan, J. Pika, Free-radical redox reactions of uranium ions in sulphuric acid solutions, Can. J. Chem. 64 (1986) 314–320.
[81] L.F. Bao, J.J. Han, H.F. Wang, R.R. Liu, M.Q. Qiu, B.W. Hu, High efficient photoreduction of U(VI) by a new synergistic photocatalyst of Fe_3O_4 nanoparticle on GO/g-C3N4 composites, J. Mater. Res. Technol. 18 (2022) 4248–4255.
[82] K.W. Kim, J.T. Hyun, K.Y. Lee, E.H. Lee, K.W. Lee, K.C. Song, J.K. Moon, Effects of the different conditions of uranyl and hydrogen peroxide solutions on the behavior of the uranium peroxide precipitation, J. Hazard. Mater. 193 (2011) 52–58.
[83] K.W. Kim, K.Y. Lee, Y.J. Baek, D.Y. Chung, E.H. Lee, J.K. Moon, Evaluation of the stability of precipitated uranyl peroxide and its storage characteristics in solution, J. Nucl. Sci. Technol. 53 (2016) 263–270.